



PERGAMON

Available online at www.sciencedirect.com

SCIENCE @ DIRECT®

Engineering Fracture Mechanics 70 (2003) 1885–1912

Engineering
Fracture
Mechanics

www.elsevier.com/locate/engfracmech

Cohesive fracture modeling of elastic–plastic crack growth in functionally graded materials

Zhi-He Jin, Glaucio H. Paulino, Robert H. Dodds Jr. *

Department of Civil and Environmental Engineering, University of Illinois at Urbana—Champaign, 2129 Newmark Laboratory, MC-250, 205 North Mathews Avenue, Urbana, IL 61801-2397, USA

Received 19 July 2002; received in revised form 6 January 2003; accepted 8 January 2003

Abstract

This work investigates elastic–plastic crack growth in ceramic/metal functionally graded materials (FGMs). The study employs a phenomenological, cohesive zone model proposed by the authors and simulates crack growth by the gradual degradation of cohesive surfaces ahead of the crack front. The cohesive zone model uses six material-dependent parameters (the cohesive energy densities and the peak cohesive tractions of the ceramic and metal phases, respectively, and two cohesive gradation parameters) to describe the constitutive response of the material in the cohesive zone. A volume fraction based, elastic–plastic model (extension of the original Tamura–Tomota–Ozawa model) describes the elastic–plastic response of the bulk background material. The numerical analyses are performed using WARP3D, a fracture mechanics research finite element code, which incorporates solid elements with graded elastic and plastic properties and interface-cohesive elements coupled with the functionally graded cohesive zone model. Numerical values of volume fractions for the constituents specified at nodes of the finite element model set the spatial gradation of material properties with isoparametric interpolations inside interface elements and background solid elements to define pointwise material property values. The paper describes applications of the cohesive zone model and the computational scheme to analyze crack growth in a single-edge notch bend, SE(B), specimen made of a TiB/Ti FGM. Cohesive parameters are calibrated using the experimentally measured load versus average crack extension (across the thickness) responses of both Ti metal and TiB/Ti FGM SE(B) specimens. The numerical results show that with the calibrated cohesive gradation parameters for the TiB/Ti system, the load to cause crack extension in the FGM is much smaller than that for the metal. However, the crack initiation load for the TiB/Ti FGM with reduced cohesive gradation parameters (which may be achieved under different manufacturing conditions) could compare to that for the metal. Crack growth responses vary strongly with values of the exponent describing the volume fraction profile for the metal. The investigation also shows significant crack tunneling in the Ti metal SE(B) specimen. For the TiB/Ti FGM system, however, crack tunneling is pronounced only for a metal-rich specimen with relatively smaller cohesive gradation parameter for the metal.

© 2003 Elsevier Science Ltd. All rights reserved.

Keywords: Elastic–plastic crack growth; Cohesive zone model; Functionally graded material (FGM); Graded finite element; 3-D finite element analysis

* Corresponding author. Tel.: +1-217-333-3276; fax: +1-217-333-9469.

E-mail address: r-dodds@uiuc.edu (R.H. Dodds Jr.).

1. Introduction

Advances in material synthesis technologies have spurred the development of a new class of materials, called functionally graded materials (FGMs), with promising applications in aerospace, transportation, energy, electronics and biomedical engineering [1–3]. An FGM comprises a multi-phase material with volume fractions of the constituents varying gradually in a pre-determined (designed) profile, thus yielding a nonuniform microstructure in the material with continuously graded properties. In applications involving severe thermal gradients (e.g. thermal protection systems), FGMs exploit the heat, oxidation and corrosion resistance typical of ceramics, and the strength, ductility and toughness typical of metals. Damage tolerance and defect assessments for structural integrity of FGM components require knowledge of the fracture behavior of FGMs. For ceramic/metal FGMs, cracks generally nucleate near the ceramic surface exposed to the environment and then grow towards the metal side. When a crack extends into the metal rich region, the substantial plastic deformation in the background FGM invalidates simple crack growth models [4,5] based on linear-elastic crack tip analysis [6,7].

This work describes an investigation of crack growth in ceramic/metal FGMs undergoing plastic deformation in the background (bulk) material. The present study focuses on three-dimensional (3-D) numerical modeling of elastic–plastic crack growth and utilizes results of recent experimental studies on fracture in ceramic/metal FGMs [8] for parameter calibration. The plasticity formulation follows a composite model proposed by Tamura et al. [9] (referred to as the TTO model henceforth), which has been employed in the study of plastic deformation of FGMs in [8,10,11]. The simulation of crack growth involves the gradual degradation of surfaces along a cohesive zone ahead of the crack. The cohesive zone approach proves to be a convenient and effective method to simulate and analyze crack growth in ductile and quasi-brittle materials. In a cohesive zone model, a narrow-band termed a cohesive zone, or process zone, exists ahead of the crack front. Material behavior in the cohesive zone follows a nonlinear cohesive constitutive law which relates the cohesive traction to the relative displacements of the adjacent cohesive surfaces. Material separation and thus crack growth occurs as the progressive decay of the cohesive tensile and shear tractions across the cohesive surfaces. Dugdale [12] first proposed a cohesive type model to study ductile fracture in a thin sheet of mild steel. Cohesive zone models have been extended to study fracture processes in quasi-brittle materials such as concrete (see, e.g., [13,14]), ductile metals (see, e.g., [15,16]), and metal matrix composites [17]. In a recent work, Jin et al. [18] proposed a new phenomenological cohesive zone model for two phase FGMs, and used the model to investigate crack growth in compact tension, C(T), and single-edge notched bend, SE(B), specimens made of a titanium/titanium monoboride (Ti/TiB) FGM without considering plastic deformation in the background material.

While two-dimensional (2-D) models approximate the behavior of “very thick” (plane strain) or “very thin” (plane stress) cracked structures, 3-D models describe more realistically the elastic–plastic stress and deformation states in cracked test specimens and structural components. Moreover, 3-D analyses enable modeling of crack tunneling phenomenon which becomes significant in common laboratory specimens and in components with surface breaking defects. Here we apply a computational framework of 3-D solid and interface-cohesive elements to analyze elastic–plastic crack growth in ceramic/metal FGMs using the new cohesive zone model for FGMs of Ref. [18].

The paper is organized as follows. Section 2 reviews the elastic–plastic model for two-phase composites, including FGMs, proposed by Tamura et al. [9] (TTO model). We describe an extension of this model to incorporate more realistic power-law hardening behavior of the metal and metal-rich background material. Section 3 summarizes a new phenomenological cohesive zone model for FGMs, which was recently presented by the authors [18]. Section 4 describes the 3-D finite element formulation with graded solid and interface-cohesive elements tailored for applications to FGMs. Section 5 describes the procedures to calibrate the cohesive parameters and presents results of a parametric study of elastic–plastic crack growth analyses for an SE(B) specimen made of a TiB/Ti FGM system. Finally, Section 6 provides some concluding remarks.

2. Stress–strain curves for ceramic/metal FGMs

While the classical Hooke's law describes the linear-elastic response of FGMs with the elastic properties evaluated approximately by micromechanics models for conventional composites, determination of the elastic–plastic behavior of FGMs remains a challenging task. Previous studies [8,10,11] have adopted the J_2 flow theory for ceramic/metal FGMs and evaluated the material properties (yield stress and tangent modulus) using the volume fraction based model proposed by Tamura et al. [9] (TTO model). The present study also uses the J_2 flow theory with isotropic hardening and extends the TTO model to describe the elastic–plastic behavior of the background ceramic/metal FGMs.

The TTO model relates the uniaxial stress, σ , and strain, ε , of a two-phase composite to the corresponding average uniaxial stresses and strains of the two constituent materials by

$$\sigma = V_1\sigma_1 + V_2\sigma_2, \quad \varepsilon = V_1\varepsilon_1 + V_2\varepsilon_2, \quad (1)$$

where σ_i and ε_i ($i = 1, 2$) denote the average stresses and strains of the constituent phases, respectively, and V_i ($i = 1, 2$) define the volume fractions. The TTO model introduces an additional parameter q as follows:

$$q = \frac{\sigma_1 - \sigma_2}{|\varepsilon_1 - \varepsilon_2|}, \quad 0 < q < \infty. \quad (2)$$

The parameter q represents the ratio of stress to strain transfer. Its value depends on the constituent material properties and the microstructural interaction in the composite. For example, $q \rightarrow \infty$ if the constituent elements deform identically in the loading direction, while $q = 0$ if the constituent elements experience the same stress level. In general, the constituent elements in a composite undergo neither equal strain nor equal stress due to the complicated microstructure (variations in particle shape, orientation, volume fraction and so on). A nonzero finite value of q approximately reflects those effects. Note that

$$\sigma_i = E_i\varepsilon_i \quad (i = 1, 2), \quad (3)$$

where E_i ($i = 1, 2$) are the Young's moduli of the constituent phases. The Young's modulus, E , of the composite may be obtained from (1)–(3) as follows:

$$E = \left[V_2E_2 \frac{q + E_1}{q + E_2} + (1 - V_2)E_1 \right] / \left[V_2 \frac{q + E_1}{q + E_2} + (1 - V_2) \right]. \quad (4)$$

The Poisson's ratio, ν , of the composite just follows a rule of mixtures in the TTO model

$$\nu = V_1\nu_1 + V_2\nu_2, \quad (5)$$

where ν_i ($i = 1, 2$) are the Poisson's ratios of the constituent phases.

For applications involving plastic deformation of ceramic/metal (brittle/ductile) composites, the TTO model assumes that the composite yields once the metal constituent yields. The yield stress of the composite, σ_Y , is thus determined as follows:

$$\sigma_Y(V_2) = \sigma_0 \left[V_2 + \frac{q + E_2}{q + E_1} \frac{E_1}{E_2} (1 - V_2) \right], \quad (6)$$

where σ_0 denotes the yield stress of the metal (phase 2). The above equation indicates that the yield stress of the composite depends on the yield stress of the metal, the volume fraction of the metal, the Young's moduli of the constituent phases, and the parameter q . For an idealized bilinear model of the metal with a tangent modulus H_2 , the TTO model predicts that the composite also follows a bilinear response with the tangent modulus H given by

$$H = \left[V_2H_2 \frac{q + E_1}{q + H_2} + (1 - V_2)E_1 \right] / \left[V_2 \frac{q + E_1}{q + H_2} + (1 - V_2) \right]. \quad (7)$$

For many structural metals, the simplistic bilinear model does not capture adequately the variation in strain hardening rate under increased plastic flow. Here we adopt a more descriptive power-law behavior for the metal and approximate the stress–strain curve of the composite also using a power law model. Therefore, the stress–strain curves of the metal and composite beyond the yield points have the form

$$\varepsilon_2 = \varepsilon_0 \left(\frac{\sigma_2}{\sigma_0} \right)^{n_0}, \quad \sigma_2 \geq \sigma_0 \tag{8}$$

and

$$\varepsilon = \varepsilon_Y \left(\frac{\sigma}{\sigma_Y} \right)^n, \quad \sigma \geq \sigma_Y, \tag{9}$$

respectively, where $\varepsilon_0 = \sigma_0/E_2$ and $\varepsilon_Y = \sigma_Y/E$ are the yield strains of the metal and composite, respectively, and n_0 and n are the hardening exponents of the metal and composite, respectively. Eliminating σ_1, ε_1 and ε_2 in Eqs. (1), (2), (3)($i = 1$) and (8), we obtain the following parametric equations to determine the stress–strain (σ – ε) curve for the composite:

$$\begin{aligned} \frac{\varepsilon}{\varepsilon_Y} &= \frac{V_1 E}{q + E_1} \frac{\sigma_2}{\sigma_Y} + \frac{(q + V_2 E_1) E}{(q + E_1) E_2} \frac{\sigma_0}{\sigma_Y} \left(\frac{\sigma_2}{\sigma_0} \right)^{n_0}, \\ \frac{\sigma}{\sigma_Y} &= \frac{V_2 q + E_1}{q + E_1} \frac{\sigma_2}{\sigma_Y} + \frac{V_1 q E_1}{(q + E_1) E_2} \frac{\sigma_0}{\sigma_Y} \left(\frac{\sigma_2}{\sigma_0} \right)^{n_0}. \end{aligned} \tag{10}$$

Fig. 1 shows the schematic of the stress–strain curve of the composite described by this extension of the TTO model. When the metal volume fraction $V_2 = 1$, Eq. (10) reduce to

$$\frac{\varepsilon}{\varepsilon_Y} = \left(\frac{\sigma_2}{\sigma_0} \right)^{n_0}, \quad \frac{\sigma}{\sigma_Y} = \frac{\sigma_2}{\sigma_Y}, \tag{11}$$

which is the power-law model for the metal because $\sigma_Y = \sigma_0$ and $\varepsilon_Y = \varepsilon_0$ when $V_2 = 1$.

Notice that the composite σ – ε curve determined from the above equations does not follow the power function (9). A least squares method determines n when we approximate (10) by (9). Fig. 2 shows the normalized stress (σ/σ_0) versus normalized strain ($\varepsilon/\varepsilon_0$) curves from Eq. (10) as well as the power-law approximations (9) for a TiB/Ti composite with the material properties of TiB and Ti listed in Table 1 and a

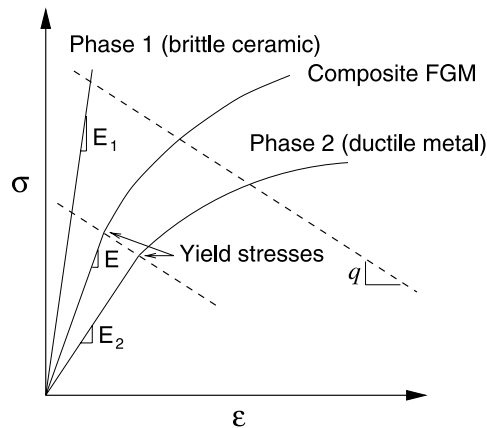


Fig. 1. Schematic of the power-law stress–strain curve of the extended TTO model.

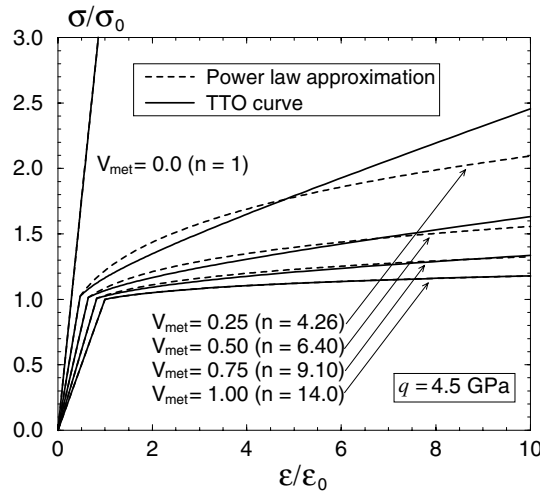


Fig. 2. Uniaxial stress–strain curve of the extended TTO model and the power-law approximation ($q = 4.5$ GPa).

Table 1
Material properties of Ti and TiB

Materials	Young's modulus (GPa)	Poisson's ratio	Yield stress (MPa)	Hardening exponent	Critical J -integral (J_{IC}) (kJ/m ²)
Ti	107	0.34	450	14	24 ^a
TiB	375	0.14			0.11

^a Estimated from the experimental crack initiation load.

q value of 4.5 GPa. The power-law stress–strain curves agree very well with the extended TTO curves from Eq. (10) when the metal volume fraction (V_{met}) is large. With the decrease of metal volume fraction, the power-law approximation deviates gradually from the TTO curve. We expect that this deviation from the TTO curve will not produce significant differences in the crack growth behavior predictions for the TiB/Ti FGM SE(B) specimen considered in Section 5—the numerical results in Section 5.3.2 show that the load versus crack extension responses exhibit only small sensitivity to the parameter q that also influences the TTO curves as shown in Fig. 3.

Fig. 3 shows the normalized stress versus normalized strain curves for the TiB/Ti composite obtained using the power-law TTO model with various values of parameter q and the metal volume fraction. Fig. 4 shows the experimental stress–strain curve of Ti [19]. Fig. 3(a) shows that for a fixed value of the metal volume fraction, V_{met} , a larger q leads to a stiffer composite (smaller n). Fig. 3(b) shows that for a fixed value of q , a larger metal volume fraction leads to a more compliant composite (larger n). Note the potentially strong role of the parameter q in the TTO model. In an average sense, the value of q reflects the composition and the complex microscale interaction of the constituents in an FGM. In practice, q may be approximately determined by experimental calibration of tensile tests performed on monolithic composite specimens. For example, a value of $q = 4.5$ GPa has been used for an Al_2O_3/Ni FGM [10,11] and for a TiB/Ti FGM [8]. This study concentrates on a TiB/Ti FGM and, because sufficient experimental data remains unavailable for the calibration of q , we perform a sensitivity study to quantify the effect of q on the elastic–plastic crack growth behavior for the specific TiB/Ti FGM.

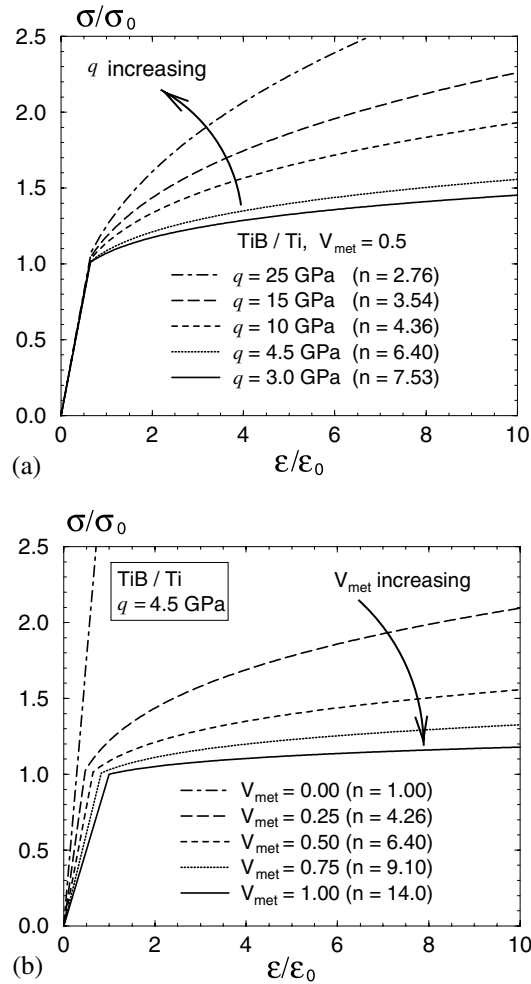


Fig. 3. Uniaxial stress–strain curves of the extended power-law TTO model for a TiB/Ti composite; (a) effect of parameter q ; (b) effect of volume fractions. Exponent (n) computed using least-squares procedure. σ_0 = yield stress of metal, ϵ_0 = yield strain of metal, see also Table 1.

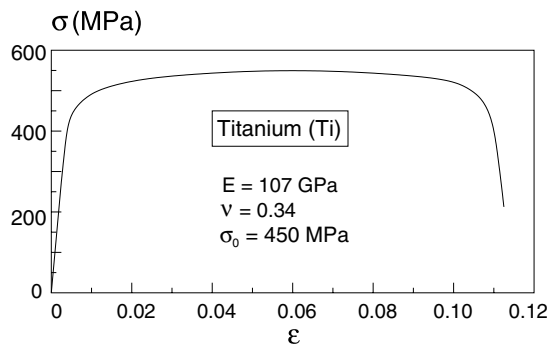


Fig. 4. Experimental stress–strain curve of titanium (Ti) [19].

3. Cohesive zone model for FGMs

While the cohesive zone approach has proven a convenient and effective method to simulate and analyze crack growth in homogeneous materials, generalization of the cohesive zone concept to model fracture in FGMs represents a challenging task because of the complicated microstructures and the related failure mechanisms in FGMs. Jin et al. [18] proposed a volume fraction based, phenomenological cohesive fracture model suitable for engineering scale applications. Such volume fraction based formulae have been used previously to calculate Young’s modulus and the plastic tangent modulus of FGMs [10,11].

This section thus reviews and discusses the phenomenological cohesive zone model for ceramic/metal FGMs proposed in Ref. [18]. The description adopts a general 3-D formulation suitable for mixed-mode fracture although the numerical results in Section 5 illustrate only mode I fracture behavior. Under 3-D mixed mode fracture conditions, let $(\delta_n, \delta_{s1}, \delta_{s2})$ denote the normal and two tangential components of the displacement jump across the cohesive surfaces, respectively. The corresponding normal and two shear cohesive tractions across the surfaces are then $(\sigma_n, \sigma_{s1}, \sigma_{s2})$, respectively. In the present study, we assume that the resistance of the cohesive surfaces to relative sliding remains isotropic in the cohesive (tangent) plane. We may thus use the overall tangential displacement jump, δ_s , and the overall shear traction, σ_s , defined by

$$\delta_s = \sqrt{\delta_{s1}^2 + \delta_{s2}^2}, \tag{12}$$

$$\sigma_s = \sqrt{\sigma_{s1}^2 + \sigma_{s2}^2}. \tag{13}$$

In a 3-D setting, Camacho and Ortiz [20] introduced an effective opening displacement jump, δ_{eff} , across the cohesive surfaces and an effective cohesive traction, σ_{eff} as follows:

$$\delta_{\text{eff}} = \sqrt{\delta_n^2 + \eta^2 \delta_s^2}, \tag{14}$$

$$\sigma_{\text{eff}} = \sqrt{\sigma_n^2 + \eta^{-2} \sigma_s^2}, \tag{15}$$

where the parameter η assigns different weights to the opening and sliding displacements (η is usually taken as $\sqrt{2}$).

With the introduction of the above *effective* traction and displacement, a free energy potential of the cohesive zone in a ceramic/metal FGM is assumed to exist in the following volume fraction based form [18]:

$$\phi(\mathbf{x}, \delta_{\text{eff}}, \kappa) = \frac{V_{\text{met}}(\mathbf{x})}{V_{\text{met}}(\mathbf{x}) + \beta_{\text{met}}[1 - V_{\text{met}}(\mathbf{x})]} \phi_{\text{met}}(\delta_{\text{eff}}, \kappa) + \frac{1 - V_{\text{met}}(\mathbf{x})}{1 - V_{\text{met}}(\mathbf{x}) + \beta_{\text{cer}} V_{\text{met}}(\mathbf{x})} \phi_{\text{cer}}(\delta_{\text{eff}}, \kappa), \tag{16}$$

where $V_{\text{met}}(\mathbf{x})$ denotes the volume fraction of the metal, $\mathbf{x} = (x_1, x_2, x_3)$, κ is an internal variable describing the irreversible processes of decohesion, $\beta_{\text{met}} (\geq 1)$ and $\beta_{\text{cer}} (\geq 1)$ are two cohesive gradation parameters, which, together with the metal volume fraction (V_{met}), describe the transition of the failure mechanism from pure ceramic to pure metal (operative in the interconnecting region which has no distinct matrix and inclusion phases). Under the loading conditions (described by κ), the free energy potentials for the metal and ceramic phases, ϕ_{met} and ϕ_{cer} , are given by

$$\phi_{\text{met}}(\delta_{\text{eff}}, \kappa) = e\sigma_{\text{met}}^c \delta_{\text{met}}^c \left[1 - \left(1 + \frac{\delta_{\text{eff}}}{\delta_{\text{met}}^c} \right) \exp\left(-\frac{\delta_{\text{eff}}}{\delta_{\text{met}}^c}\right) \right], \tag{17}$$

$$\phi_{\text{cer}}(\delta_{\text{eff}}, \kappa) = e\sigma_{\text{cer}}^c \delta_{\text{cer}}^c \left[1 - \left(1 + \frac{\delta_{\text{eff}}}{\delta_{\text{cer}}^c} \right) \exp\left(-\frac{\delta_{\text{eff}}}{\delta_{\text{cer}}^c}\right) \right], \tag{18}$$

respectively. The cohesive tractions of the metal and ceramic phases follow from the above potentials [15,16,21–23]

$$\sigma_{\text{met}} = \frac{\partial \phi_{\text{met}}}{\partial \delta_{\text{eff}}} = e \sigma_{\text{met}}^c \left(\frac{\delta_{\text{eff}}}{\delta_{\text{met}}^c} \right) \exp\left(-\frac{\delta_{\text{eff}}}{\delta_{\text{met}}^c}\right), \quad (19)$$

$$\sigma_{\text{cer}} = \frac{\partial \phi_{\text{cer}}}{\partial \delta_{\text{eff}}} = e \sigma_{\text{cer}}^c \left(\frac{\delta_{\text{eff}}}{\delta_{\text{cer}}^c} \right) \exp\left(-\frac{\delta_{\text{eff}}}{\delta_{\text{cer}}^c}\right), \quad (20)$$

where $e = \exp(1)$, σ_{met}^c the maximum cohesive traction of the metal phase, δ_{met}^c the value of δ_{eff} at $\sigma_{\text{eff}} = \sigma_{\text{met}}^c$, σ_{cer}^c the maximum cohesive traction of the ceramic phase, and δ_{cer}^c the value of δ_{eff} at $\sigma_{\text{eff}} = \sigma_{\text{cer}}^c$. Here, we have adopted a computationally convenient, exponential form for the free energy potentials for both metal and ceramic phases. Previous studies [24] have shown that, in general, the shape of the cohesive traction–separation (σ – δ) curve has a smaller role than the cohesive energy density and the maximum cohesive traction on predictions of crack growth behavior in ductile metals. For brittle ceramic materials, the shape of cohesive traction–separation curve may play a significant role in determining the peak loads [25]. For ceramic/metal FGMs of interest here, ductile failure mechanisms of the metal phase appear to govern the behavior of cracked components [18]. For simplicity in these exploratory studies, we adopt the same exponential form to describe the cohesive response of the ceramic phase. However, as the failure processes in ceramic/metal FGMs become better understood, the FGM cohesive zone model of the type described below may be revisited accordingly, especially for the ceramic/metal interconnecting region.

The effective cohesive traction follows from the derivative of the potential (16) with respect to the effective opening displacement jump

$$\begin{aligned} \sigma_{\text{eff}} &= \frac{\partial \phi}{\partial \delta_{\text{eff}}} \\ &= \frac{V_{\text{met}}(\mathbf{x})}{V_{\text{met}}(\mathbf{x}) + \beta_{\text{met}}[1 - V_{\text{met}}(\mathbf{x})]} e \sigma_{\text{met}}^c \left(\frac{\delta_{\text{eff}}}{\delta_{\text{met}}^c} \right) \exp\left(-\frac{\delta_{\text{eff}}}{\delta_{\text{met}}^c}\right) \\ &\quad + \frac{1 - V_{\text{met}}(\mathbf{x})}{1 - V_{\text{met}}(\mathbf{x}) + \beta_{\text{cer}} V_{\text{met}}(\mathbf{x})} e \sigma_{\text{cer}}^c \left(\frac{\delta_{\text{eff}}}{\delta_{\text{cer}}^c} \right) \exp\left(-\frac{\delta_{\text{eff}}}{\delta_{\text{cer}}^c}\right), \\ &\text{if } \delta_{\text{eff}} = \delta_{\text{eff}}^{\text{max}} \text{ and } \dot{\delta}_{\text{eff}} \geq 0, \end{aligned} \quad (21)$$

for the loading case, and

$$\sigma_{\text{eff}} = \left(\frac{\sigma_{\text{eff}}^{\text{max}}}{\delta_{\text{eff}}^{\text{max}}} \right) \delta_{\text{eff}}, \quad \text{if } \delta_{\text{eff}} < \delta_{\text{eff}}^{\text{max}} \text{ or } \dot{\delta}_{\text{eff}} < 0, \quad (22)$$

for the unloading case, where $\sigma_{\text{eff}}^{\text{max}}$ is the value of σ_{eff} at $\delta_{\text{eff}} = \delta_{\text{eff}}^{\text{max}}$ calculated from Eq. (21). Here, the internal variable κ is chosen as $\delta_{\text{eff}}^{\text{max}}$, the maximum value of δ_{eff} attained. The cohesive law for general 3-D separations then takes the following form:

$$\begin{aligned} \sigma_n &= \frac{\partial \phi}{\partial \delta_n} = \frac{\partial \phi}{\partial \delta_{\text{eff}}} \frac{\partial \delta_{\text{eff}}}{\partial \delta_n} = \left(\frac{\sigma_{\text{eff}}}{\delta_{\text{eff}}} \right) \delta_n, \\ \sigma_s &= \frac{\partial \phi}{\partial \delta_s} = \frac{\partial \phi}{\partial \delta_{\text{eff}}} \frac{\partial \delta_{\text{eff}}}{\partial \delta_s} = \eta^2 \left(\frac{\sigma_{\text{eff}}}{\delta_{\text{eff}}} \right) \delta_s. \end{aligned} \quad (23)$$

Under mode I fracture conditions, $\delta_s = \sigma_s = 0$. Hence, $\delta_{\text{eff}} = \delta_n$ and $\sigma_{\text{eff}} = \sigma_n$. Fig. 5(a) shows the curve for $\sigma_{\text{met}}/\sigma_{\text{met}}^c$ versus $\delta_{\text{eff}}/\delta_{\text{met}}^c$. For the ceramic phase, the curve of $\sigma_{\text{cer}}/\sigma_{\text{met}}^c$ versus $\delta_{\text{eff}}/\delta_{\text{met}}^c$ is illustrated in Fig. 5(b) for various values of $\delta_{\text{cer}}^c/\delta_{\text{met}}^c$.

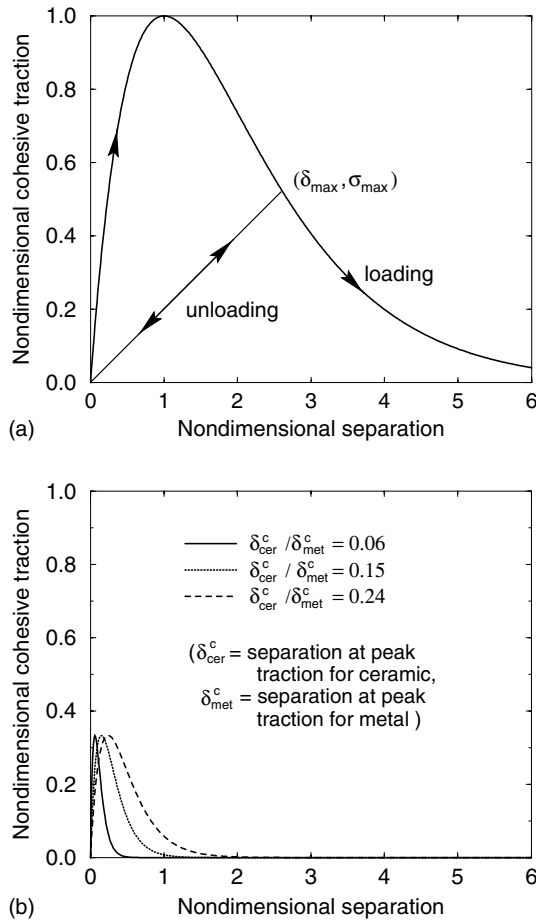


Fig. 5. Normalized cohesive traction versus nondimensional separation displacement; (a) for metal, $\sigma_{met} / \sigma_{met}^c$ versus δ / δ_{met}^c ; (b) for ceramic, $\sigma_{cer} / \sigma_{met}^c$ versus δ / δ_{met}^c (where metal/ceramic strength ratio, $\sigma_{cer}^c / \sigma_{cer}^c$, is taken to be 3).

The cohesive energy density, or the work of separation per unit area of cohesive surface, is defined by

$$\Gamma_{fgm}^c = \int_0^\infty \sigma(\delta_{eff}) d\delta_{eff}. \tag{24}$$

Substituting Eq. (21) into the above equation yields

$$\Gamma_{fgm}^c(\mathbf{x}) = \frac{V_{met}(\mathbf{x})}{V_{met}(\mathbf{x}) + \beta_{met}[1 - V_{met}(\mathbf{x})]} \Gamma_{met}^c + \frac{1 - V_{met}(\mathbf{x})}{1 - V_{met}(\mathbf{x}) + \beta_{cer}V_{met}(\mathbf{x})} \Gamma_{cer}^c, \tag{25}$$

where Γ_{met}^c and Γ_{cer}^c denote the cohesive energy densities of the metal and ceramic phases, respectively:

$$\Gamma_{met}^c = e\sigma_{met}^c\delta_{met}^c, \quad \Gamma_{cer}^c = e\sigma_{cer}^c\delta_{cer}^c. \tag{26}$$

Eq. (25) shows that the cohesive energy density for the FGM follows the same rule as that of the effective cohesive traction (21).

The cohesive zone model (21)–(23) has the following six material dependent parameters that characterize the fracture process in a ceramic/metal FGM: Γ_{met}^c and Γ_{cer}^c (local work of separation of metal and ceramic, respectively), σ_{met}^c and σ_{cer}^c (peak cohesive tractions of metal and ceramic, respectively), and β_{met} and β_{cer}

(cohesive gradation parameters). The uncoupled contribution of the metal and ceramic to the total cohesive traction in the model (21)–(23) enables separate calibration of the cohesive parameters associated with the metal and ceramic, respectively.

For the metal phase, the calibrated value of Γ_{met}^c becomes approximately the Griffith energy release rate at the onset of ductile tearing (J_{IC}) under small-scale yielding conditions (requires materials with relatively low toughness). J_{IC} exceeds Γ_{met}^c under large-scale yielding conditions due to the contribution from the background plasticity (which makes calibration more difficult). The peak cohesive traction, σ_{met}^c , generally lies between two to three times the uniaxial yield stress (see, for example, the discussion by Roy and Dodds [16] and the discussion in Section 5.3). Once Γ_{met}^c and σ_{met}^c are calibrated, the first equation of (26) yields the opening displacement δ_{met}^c at peak traction.

For the ceramic phase, no significant background nonlinear response occurs and the energy release rate corresponds directly to Γ_{cer}^c , which is usually at least two orders of magnitude smaller than Γ_{met}^c . For the TiB/Ti FGM considered in this work, $\Gamma_{\text{cer}}^c = 0.11 \text{ kJ/m}^2$ and $\Gamma_{\text{met}}^c = 24 \text{ kJ/m}^2$ (see Section 5.3.2). As a result, selection of δ_{cer}^c or σ_{cer}^c becomes insignificant in predicting crack growth behavior of ceramic/metal FGMs (the early stiffness is affected, see Section 5.6). For this phenomenological model to apply at engineering-scales, the characteristic opening displacement δ_{cer}^c is assumed to be approximately the average size of ceramic particles in the ceramic/metal FGM. The peak cohesive traction σ_{cer}^c is therefore determined from the second equation of (26). At smaller length-scales, the highly local nature of the failure mechanism contributes to the characteristic parameters of the cohesive zone model, which may lead to different material parameters and different simulation results of crack growth at the macro-scale.

The other two additional cohesive parameters introduced for FGMs, β_{met} and β_{cer} , describe approximately the overall reduction of cohesive traction (from the level predicted by the rule of mixtures) and the transition between the fracture mechanisms of the metal and ceramic phases. For crack growth in a TiB/Ti FGM without consideration of plastic deformation in the background material, the computational results [18] indicate that β_{met} plays a far more significant role than β_{cer} , which can be simply set to unity. The parameter β_{met} may be experimentally calibrated by two different schemes. The first scheme determines β_{met} by matching the predicted and measured crack growth responses in standard fracture mechanics specimens of continuously graded FGMs. If this procedure fails to generate a match between the predicted and experimentally measured crack growth responses, a second scheme could employ fracture specimens made of a monolithic composite each with a fixed volume fraction of the constituents. β_{met} is then calibrated for each volume fraction level of metal and ceramic, which comprise the continuously graded FGM specimens. Thus, β_{met} becomes a function of V_{met} . We describe and discuss the calibration of Γ_{met}^c , σ_{met}^c and β_{met} in Section 5.3.

4. Graded solid and interface elements formulation

This section describes the small-displacement formulation of both the 3-D solid element and interface-cohesive element with graded material properties (graded elements). Previous studies [16,26] of crack growth in thin aluminum panels using 3-D cohesive elements show that a small-displacement scheme yields a slightly lower calibrated peak cohesive traction than the value obtained in a finite-deformation framework due to the thickness reduction effect predicted in the finite-deformation approach. The present study considers relatively thick Ti metal and TiB/Ti FGM specimens (the ratios of thickness to depth for the SE(B) specimens studied are around 0.5). Therefore, the thickness reduction effect may not be significant for these specimens and the following numerical studies adopt small-displacement theory.

For the solid elements which model the bulk (background) FGM, the J_2 flow theory with isotropic hardening describes the material behavior and the TTO model characterizes the material properties (Young's modulus, Poisson's ratio, yield stress and power hardening exponent) within the element. For the interface-cohesive element, the material behavior and properties follow the functionally graded cohesive

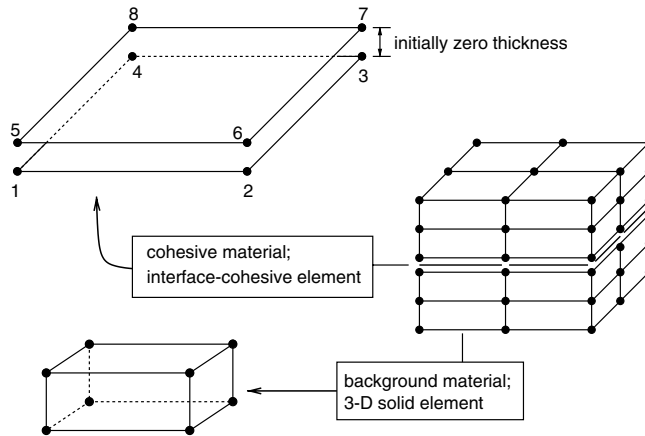


Fig. 6. Interface-cohesive and 3-D solid elements.

law (21)–(23). Fig. 6 shows the 3-D interface-cohesive and solid elements used in the present work. The interface-cohesive element consists of two, four-node bilinear isoparametric surfaces. Nodes 1–4 lie on one surface of the element while nodes 5–8 reside on the opposite surface. The two surfaces initially occupy the same location (i.e. zero thickness). When the whole body deforms, the two surfaces undergo both normal and tangential displacements relative to each other, which generate the cohesive tractions according to the constitutive relations (21)–(23).

4.1. FGM 3-D solid element

Now first consider the tangent stiffness matrix of the isoparametric solid element. Denote by $N_i(\xi, \eta, \zeta)$ ($i = 1, 2, \dots, m$) the standard shape functions of the solid element [27], where m is the number of the nodes of the element. The element tangent stiffness matrix is given by

$$\mathbf{K}_T = \int_{-1}^1 \int_{-1}^1 \int_{-1}^1 \mathbf{B}^T \mathbf{D}_T \mathbf{B} J_0 d\xi d\eta d\zeta, \tag{27}$$

where \mathbf{B} is the strain–displacement matrix, J_0 is the usual Jacobian of the transformation between parametric (ξ, η, ζ) and Cartesian coordinates (x_1, x_2, x_3) , and the superscript T denotes transpose. \mathbf{D}_T is the elastic–plastic, tangent stiffness matrix consistent with an elastic predictor and radial return stress update scheme. To alleviate mesh locking associated with fully integrated bilinear elements at relatively large plastic deformation, the \mathbf{B} matrix in (27) is replaced with the (\mathbf{B} -bar) $\bar{\mathbf{B}}$ matrix [28,29]. For FGMs, the consistent \mathbf{D}_T matrix varies with spatial position due to the position-dependent material elastic and flow properties. Kim and Paulino [30] presented a generalized isoparametric formulation (GIF) to calculate the elastic properties within an element. This study further evaluates the plastic properties within an element using this approach. We thus have

$$\text{elastic: } E = \sum_{i=1}^m N_i E_i, \quad \nu = \sum_{i=1}^m N_i \nu_i, \tag{28}$$

$$\text{plastic: } \sigma_Y = \sum_{i=1}^m N_i \sigma_{Yi}, \quad n = \sum_{i=1}^m N_i n_i, \tag{29}$$

where E_i , ν_i , σ_{Yi} and n_i ($i = 1, 2, \dots, m$) are the values of Young's modulus, Poisson's ratio, the yield stress and the power hardening exponent at the nodal points, respectively. Eqs. (28) and (29) evaluate the FGM properties within general higher order (quadratic) elements. For the first order linear elements (8-node brick), the computational procedures average the FGM properties in each element from the nodal values thereby assigning constant properties over each element. This prevents potential shear locking under homogeneous strain states (a procedure similar to that adopted in ABAQUS [31] to treat thermal strains for first order elements). Moreover, Kim and Paulino [32] have also elaborated upon this modeling procedure for FGMs.

4.2. FGM interface-cohesive element

For the interface-cohesive element, the tangent stiffness matrix is given by [16],

$$\mathbf{K}_{\text{coh}} = \int_{-1}^1 \int_{-1}^1 \mathbf{B}_{\text{coh}}^T \mathbf{D}_{\text{coh}} \mathbf{B}_{\text{coh}} J_0 d\eta d\zeta, \quad (30)$$

where \mathbf{B}_{coh} extracts the relative displacement jumps within the cohesive element from the nodal displacements [16], and J_0 is the Jacobian of the transformation between parametric (η, ζ) and Cartesian coordinates (s_1, s_2) in the tangent plane of the cohesive element. \mathbf{D}_{coh} is the tangent modulus matrix of the cohesive law (21)–(23), details of which can be found in an earlier paper by the authors [18]. The \mathbf{D}_{coh} matrix depends on spatial position through the graded volume fraction of the metal phase, V_{met} , in a ceramic/metal FGM. This study approximates V_{met} by the following standard interpolation:

$$V_{\text{met}} = \sum_{i=1}^4 N_i V_{\text{met}}^i, \quad (31)$$

where V_{met}^i ($i = 1, 2, 3, 4$) are the values of V_{met} at the nodal points of the interface-cohesive elements. Again, Eq. (31) applies for general higher order elements. For first order linear elements, the volume fraction is averaged in each element from the nodal values—see related comments at the end of Section 4.1 and also in Ref. [32].

5. Crack growth in a TiB/Ti FGM

5.1. Specimen geometries, materials, and finite element models

We performed 3-D numerical analyses of elastic–plastic crack growth for both Ti metal and TiB/Ti FGM SE(B) specimens containing an initially sharp, straight crack front over the thickness. Fig. 7 shows the geometry of the SE(B) specimens used in the crack growth study. A layered TiB/Ti FGM SE(B) specimen has been recently tested as described in [8] and a Ti metal only SE(B) specimen tested as described in [19]. The company CERCOM Inc. developed the TiB/Ti FGM system in a layered structural form for potential armor applications [33]. Table 1 lists the material properties for TiB and Ti (data from Refs. [8,19] except the hardening exponent and the critical J -integral (J_{IC}) for Ti). A least squares approximation gives a hardening exponent of 14 for Ti (n_0 in Eq. 8). The experimental load versus crack growth responses obtained in [8,19] are used in this study to estimate J_{IC} for Ti, and to calibrate values of the cohesive parameters and the q -parameter for the bulk TiB/Ti FGM.

Table 2 summarizes the geometric parameters of the SE(B) specimens used in both the present and the experimental studies reported in [8,19]. In the numerical analyses of the specimens, the FGM composition varies from 100% ceramic at the cracked surface to 100% metal at the uncracked surface. Thus the volume

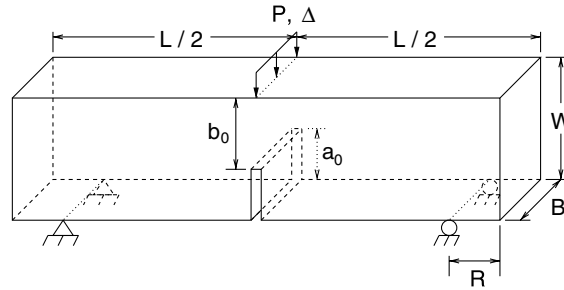


Fig. 7. SE(B) specimen geometry.

Table 2
Geometric parameters of SE(B) specimens

Specimen	L (mm)	W (mm)	B (mm)	a_0/W	R (mm)
SE(B) (FGM)	79.4	14.7	7.4	0.3	10.2
SE(B) (Ti)	101.6	25.5	13.3	0.5	6.4

fraction of metal (V_{met}) varies from zero at the cracked surface to one at the uncracked surface. We approximate the volume fraction of the metal phase using a simple power function, i.e.

$$V_{\text{met}}(y) = \left(\frac{y + a_0}{b_0 + a_0} \right)^p, \quad -a_0 \leq y \leq b_0, \quad (32)$$

where p is the power exponent, y is the spatial direction of gradation, and the material properties are graded in the interval $[-a_0, b_0]$ (see Fig. 8).

Fig. 8 shows the longitudinal cross-section of the 3-D finite element model of the TiB/Ti FGM specimen. The finite element mesh for the Ti metal specimen is similar to that shown in this figure. The finite element models consist of 8-node isoparametric solid elements and 8-node interface-cohesive elements. Due to symmetry considerations, we model only one-quarter of each specimen ($x \geq 0, z \geq 0$). Interface-cohesive elements are placed only over the initial uncracked ligament and have uniform size of 0.1 mm for both the Ti metal only and the TiB/Ti FGM specimens. The finite element model has 10 uniform layers of elements over the half thickness with 32,769 nodes and 28,350 elements for the Ti metal specimen. The model for the smaller FGM specimen has 24,475 nodes and 21,100 elements.

5.2. Finite element analysis

The numerical solutions are generated using WARP3D [34], a research code for nonlinear fracture mechanics. WARP3D employs an incremental-iterative, implicit formulation for analyses of fracture models subjected to quasi-static and dynamic loading. Besides the conventional solid and interface-cohesive elements for homogeneous materials, this code also incorporates solid elements with graded elastic and plastic properties and interface-cohesive elements with graded cohesive traction and cohesive energy density. While conventional finite elements with constant material properties in each element have been used for analyses of FGMs with relatively fine meshes [35], graded elements include the effect of gradation at the element level and can substantially improve the solution quality based on the same mesh density, especially for higher-order graded elements [32].

With the cohesive zone model (21)–(23), the average (effective) traction in a cohesive element ahead of the crack front in the crack growth direction first experiences an increase, reaches its peak value, and then

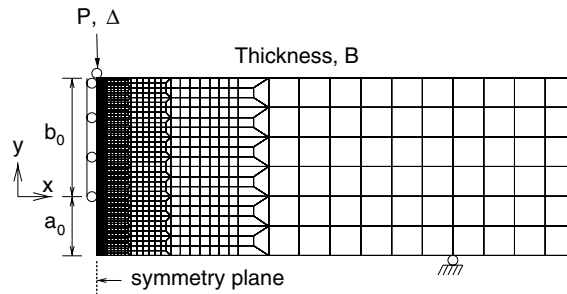


Fig. 8. Longitudinal cross-section of typical 3-D mesh for analyses of SE(B) specimens (10 layers of elements over the half thickness).

decreases. When the traction reduces to a specified small value (usually 5–10% of the peak cohesive traction), or equivalently, when the average effective opening displacement in the cohesive element increases to a relative large value (usually 5–6 times of the effective opening displacement at the peak traction), WARP3D removes the interface-cohesive element from the model thereby growing the crack with an extension of the deleted cohesive element area. The leading edges of the deleted cohesive elements then form the current growing crack front across the specimen width. The present finite element models for SE(B) specimens have multi-layers of elements in the thickness direction. Cohesive elements in different layers experience different tractions and are deleted at different load levels thereby forming a curved or tunneled crack front. Element extinction occurs when the average opening displacement δ_{eff} of a cohesive element reaches $5\delta_{\text{met}}^{\text{c}}$, which corresponds to a cohesive traction less than 10% of the peak value of the metal multiplied by the pointwise value of the metal volume fraction. Numerical calculations adjust $\delta_{\text{met}}^{\text{c}}$ so that the energy dissipated at $\delta = 5\delta_{\text{met}}^{\text{c}}$ in the element equals the cohesive energy $\Gamma_{\text{met}}^{\text{c}}$. Selection of $\delta_{\text{met}}^{\text{c}}$ (of the metal phase) as the controlling parameter for element extinction follows from analyses demonstrating that the metal phase largely controls fracture behavior of the FGM. In the present study, the cohesive fracture energy of TiB, for example, is less than 1% of that for Ti (see Table 1).

With the nonlinear cohesive zone model shown in Fig. 5, large load increments often specified in implicit solution methods may create an “overshoot” problem, i.e. some interface elements may miss the peak cohesive traction by passing from the pre-peak to post-peak side of the traction–separation curve within a single load increment. In such cases, the background material may not develop plastic deformation levels consistent with peak traction values in the cohesive elements. To avoid these effects, WARP3D adaptively controls the size of the global load (displacement in this study) increments to enforce the proper cohesive constitutive response. For the FGM cohesive zone model (21)–(23), the adaptive load control parameter becomes the smaller of the characteristic opening displacements $\delta_{\text{met}}^{\text{c}}$ (metal) and $\delta_{\text{cer}}^{\text{c}}$ (ceramic). The analyses use a limit of $\Delta\delta/\delta_{\text{met}}^{\text{c}}$ (or $\Delta\delta/\delta_{\text{cer}}^{\text{c}}$) = 0.3 per load increment for adaptive load control, where $\Delta\delta$ denotes the largest change of effective opening displacement δ_{eff} experienced by interface-cohesive elements in a given load increment. A previous study by Roy and Dodds [16] indicates that analyses using values of $\Delta\delta/\delta_{\text{met}}^{\text{c}} \leq 0.3$ show no differences in load versus crack extension responses for actual Al 2024-T3 C(T) and M(T) specimens.

5.3. Determination of model parameters

5.3.1. Elastic–plastic FGM properties

As outlined in Section 2, the TTO model describes both the elastic and elastic–plastic responses of the background material with the graded linear-elastic properties: Young’s modulus E , Poisson’s ratio ν , and the graded plastic flow properties: yield stress σ_{Y} and power-law hardening exponent n . The quantities E , ν ,

σ_Y and n can be evaluated from (4)–(6) and (10), respectively, with a material-dependent parameter q to be determined. As remarked at the end of Section 2, q should be calibrated to match the measured flow properties of tensile specimens taken from monolithic composites of the FGM constituents. Because such data remains unavailable for the TiB/Ti FGM, we adopt $q = 4.5$ GPa as in previous studies [8,10,11] and perform a parametric study to assess the effect of q on the calibration of cohesive gradation parameters and on the overall elastic–plastic, crack growth behavior for the TiB/Ti FGM. Results in the following subsection indicate that the load versus crack extension responses and the calibrated β_{met} for the FGM are not overly sensitive to q for the range of values considered. This somehow justifies the use of $q = 4.5$ GPa until definite experimental data becomes available.

5.3.2. Cohesive fracture properties

As mentioned in Section 3, the cohesive zone model (21)–(23) describes the graded fracture properties of the cohesive material with six model parameters to be calibrated, i.e. Γ_{met}^c and Γ_{cer}^c (local work of separation of metal and ceramic, respectively), σ_{met}^c and σ_{cer}^c (peak cohesive tractions of metal and ceramic, respectively), and β_{met} and β_{cer} (cohesive gradation parameters). The formulation for the cohesive zone model (21)–(23) enables separate calibration of cohesive parameters associated with the metal and ceramic phases (strength and fracture energy), and the two cohesive gradation parameters. For the ceramic phase, as discussed in Section 3, we assign the Griffith energy release rate to Γ_{cer}^c and the average size of ceramic particles in the ceramic/metal FGM to the critical opening displacement δ_{cer}^c in the study of crack growth behavior. The peak cohesive traction σ_{cer}^c of the ceramic is then determined from the second equation of (26). These parameters are [18]: $\Gamma_{\text{cer}}^c = 0.11$ kJ/m², $\delta_{\text{cer}}^c = 0.01$ mm, $\sigma_{\text{cer}}^c = 4$ MPa. Section 5.6 discusses the effect of σ_{cer}^c on the initial specimen response and crack growth behavior.

Next, we use the experimental results for the Ti metal SE(B) specimen ($W = 25.5$ mm, $a_0/W = 0.5$) to calibrate Γ_{met}^c and σ_{met}^c . The calibration proceeds by matching the numerically predicted crack growth response with the experimentally measured fracture behavior for the SE(B) specimen reported in [19]. The specimen is loaded by monotonically increasing displacements applied uniformly through the thickness at the specimen center-plane (*displacement controlled loading*), as shown in Fig. 7. Due to tunneling, crack extensions are nonuniform across the specimen thickness. The calibration process seeks to match the predicted, with measured, load versus *average crack extension* (across the thickness) responses.

A previous study [16] on crack growth in thin aluminum panels shows that under small scale yielding (SSY) conditions, the crack initiation load remains relatively insensitive to the peak cohesive traction, which allows calibration of the cohesive energy density by matching the predicted and measured crack initiation load. The peak cohesive traction is subsequently calibrated by best matching the predicted and measured responses over the first few millimeters of crack growth.

The above procedure provides some guidelines for the current calibration of cohesive parameters for the Ti metal. We first analyze a stationary crack model of the SE(B) specimen with no cohesive elements. Fig. 9 shows the longitudinal cross-section of the finite element model with 10 uniform layers of elements over the half thickness of the specimen. The model has 14,498 nodes and 12,210 elements with a refined mesh near the crack front. Fig. 10(a) shows the calculated load versus crack mouth opening displacement (CMOD) curve. The loads corresponding to the three points, ‘a’, ‘b’ and ‘c’ on the curve are $P = 6.7$, 9.1 and 11.5 kN (kiloNewton), respectively, and the point ‘c’ corresponds to the experimentally measured crack initiation load reported in [19]. Fig. 10(b) shows the calculated J -integral (averaged over the thickness) versus CMOD curve, where the J value corresponding to the crack initiation load is about 24 kJ/m² (point ‘c’). The J value is computed using a domain integral method available in WARP3D [34]. Fig. 11(a)–(c) show the plastic zone development at the crack front (outside surface element layer) corresponding to the three load levels ‘a’, ‘b’ and ‘c’ in Fig. 10. At the crack initiation state ‘c’, the plastic zone size satisfies the condition of SSY for the 12.75 mm remaining ligament. The nondimensional deformation parameter, $M = b_0\sigma_0/J$, equals

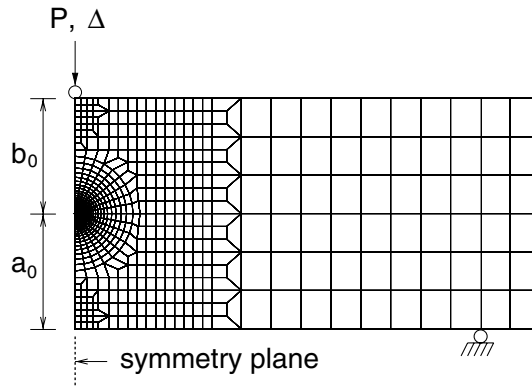


Fig. 9. Longitudinal cross-section of the 3-D mesh for analyses of the Ti SE(B) specimen (stationary crack without cohesive elements, 10 layers of elements over the half thickness).

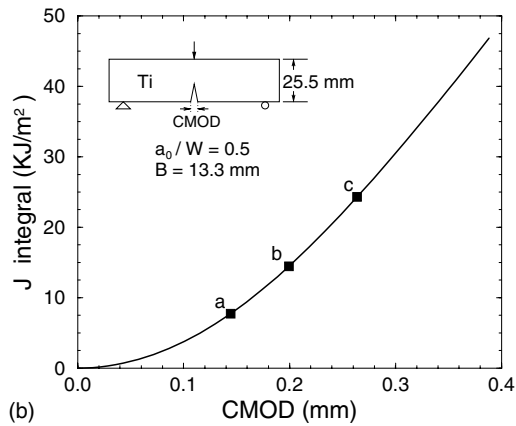
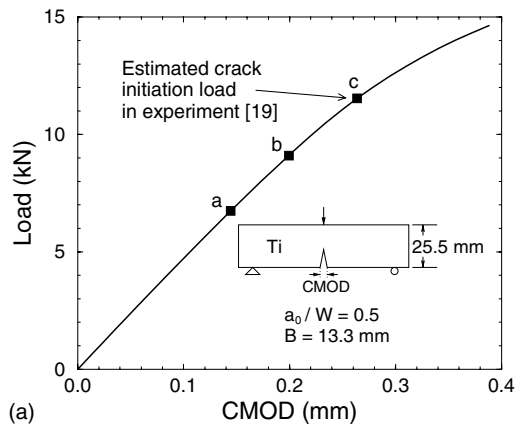


Fig. 10. (a) Computed load versus CMOD curve for the Ti SE(B) specimen with $W = 25.5$ mm (stationary crack without cohesive elements). (b) Computed J -integral versus CMOD curve for the Ti SE(B) specimen with $W = 25.5$ mm (stationary crack without cohesive elements).

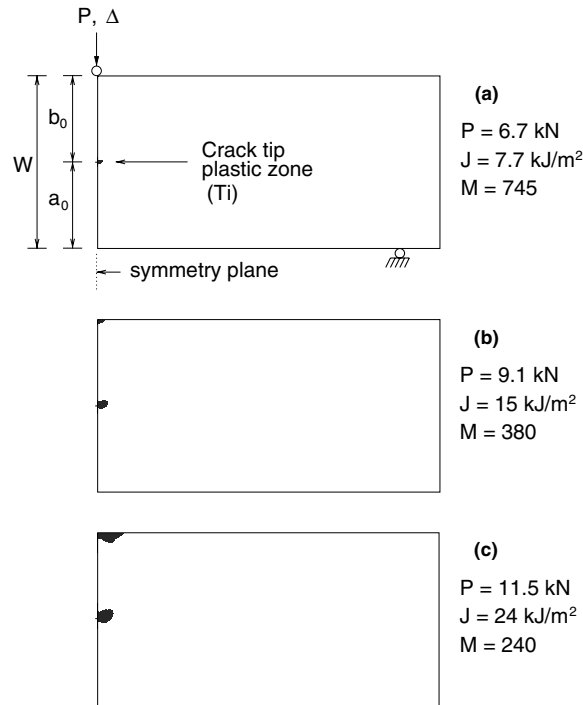


Fig. 11. Plastic zone development in the Ti SE(B) specimen with $W = 25.5 \text{ mm}$ (stationary crack without cohesive elements) corresponding to the three load levels a, b, c in Fig. 10; (a) $P = 6.7 \text{ kN}$; (b) $P = 9.1 \text{ kN}$; (c) $P = 11.5 \text{ kN}$ (nondimensional deformation parameter $M = b_0\sigma_0/J$).

240 and lies well above the value of 150 often used as the limit of SSY [36]. We thus set Γ_{met}^c as the J value at the crack initiation state 'c' (24 kJ/m^2).

After determining Γ_{met}^c , we proceed to calibrate the peak cohesive traction σ_{met}^c . The calibration procedure seeks to best match the predicted and the measured overall load versus average crack extension responses by varying σ_{met}^c . Fig. 12 shows both the predicted and the measured load versus average crack extension responses for the Ti SE(B) specimen with $W = 25.5 \text{ mm}$, $\Gamma_{\text{met}}^c = 24 \text{ kJ/m}^2$, and three values of σ_{met}^c . Clearly, $\sigma_{\text{met}}^c = 2.5\sigma_0$ coupled with the given value of Γ_{met}^c yields a reasonable match between the predicted and the measured responses, where σ_0 is the uniaxial yield stress of Ti. The calibrated value of σ_{met}^c ($2.5\sigma_0$) lies well below the limit of $3.3\sigma_0$, the maximum tensile stress that develops ahead of a stationary blunting crack tip for this Ti under plane-strain, SSY and finite deformation conditions [37]. Fig. 12 also shows the calculated load versus CMOD curve for $\sigma_{\text{met}}^c = 2.5\sigma_0$. The load first increases with increasing CMOD, reaches a peak value at which crack growth occurs, and then decreases with further increasing CMOD.

Finally, we calibrate the two cohesive gradation parameters β_{met} and β_{cer} needed to analyze crack growth in the SE(B) specimen made of the TiB/Ti FGM. For crack growth in a TiB/Ti FGM without considering plastic deformation in the background material, our previous study [18] indicates that β_{met} plays a far more significant role than β_{cer} . We therefore simply set β_{cer} to unity. As explained in Section 5.3.1, we first use $q = 4.5 \text{ GPa}$ as previous studies [8,10,11] for the purpose of calibrating β_{met} and then consider the effect of q on the calibrated β_{met} . With the known values of σ_{met}^c , Γ_{met}^c , σ_{cer}^c , Γ_{cer}^c , and β_{cer} fixed, we can proceed to calibrate β_{met} by matching the predicted, with the measured, crack initiation loads for the TiB/Ti SE(B)

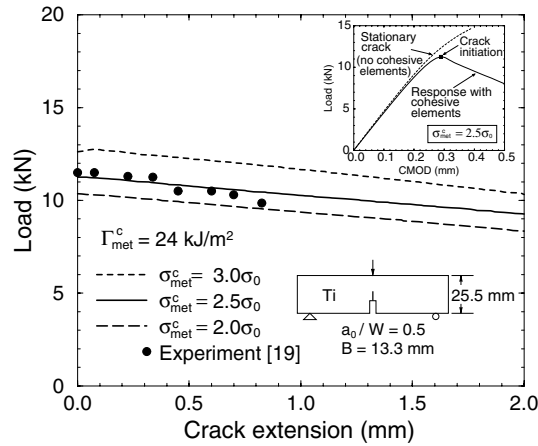
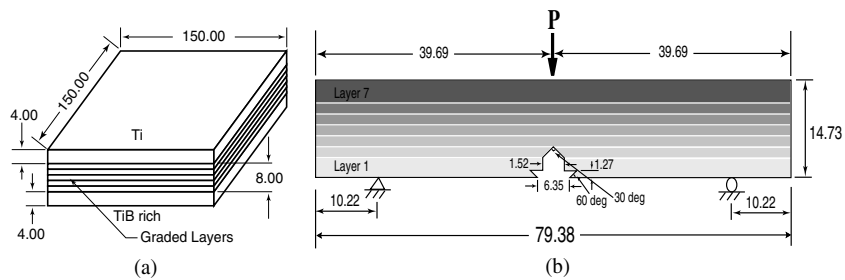


Fig. 12. Calibration of σ_{met}^c using the load versus average crack extension responses for the Ti SE(B) specimen with $W = 25.5$ mm.

specimen with $W = 14.7$ mm. In this layered TiB/Ti SE(B) specimen tested recently [8], the first layer consists of 15% Ti and 85% TiB, while the last layer (seventh layer) consists of 100% Ti. Fig. 13 shows the TiB/Ti FGM plate manufactured by CERCOM Inc. [33] and the SE(B) specimen cut for the fracture test [8]. Table 3 shows the volume fraction and the thickness of each layer in the specimen. Fig. 14 shows the variation of volume fraction of Ti in this TiB/Ti specimen. The dashed (stepped) line shows the property



Note: All dimensions are in millimeters.

Fig. 13. Seven-layer TiB/Ti FGM: (a) plate provided by CERCOM Inc. [33]; (b) fracture specimen (7.37 mm thick) cut from the plate for three-point bending test [8].

Table 3
Volume fraction and thickness distribution in the layered TiB/Ti SE(B) specimen [8]

Layer #	Thickness (mm)	TiB volume fraction (%)	Ti volume fraction (%)
1	2.515	85	15
2	1.676	79	21
3	1.778	62	38
4	1.448	47	53
5	1.753	32	68
6	2.134	15	85
7	3.429	0	100

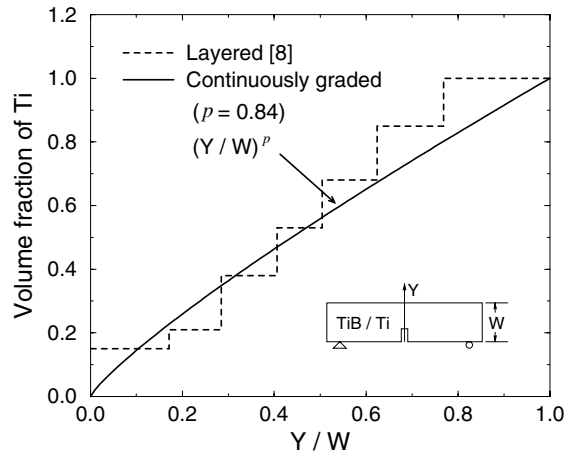


Fig. 14. Volume fractions of Ti in the TiB/Ti SE(B) specimen (dashed line from the data reported in Ref. [8]).

gradation in the experimentally tested specimen. A least squares approximation yields the power exponent $p = 0.84$ in the metal volume fraction function of Eq. (32) used in the numerical analysis.

Fig. 15 shows the calculated load versus average crack extension responses for this SE(B) specimen. Fig. 15(a) shows results for $q = 4.5$ GPa with β_{met} ranging from 17 to 20. $\beta_{\text{met}} = 18.5$ yields a crack initiation load of 0.931 kN, which approximately matches the measured one of 0.925 kN [38,39]. In Fig. 15(b), $q = 15$ GPa and β_{met} ranges from 17 to 20. Now $\beta_{\text{met}} = 18.5$ yields a crack initiation load of 0.932 kN, which also matches approximately the measured value. In Fig. 15(c), q increases to 30 GPa and β_{met} ranges from 17 to 20. Again, $\beta_{\text{met}} = 18.5$ yields a crack initiation load of 0.933 kN, which also approximately matches the measured value. These results indicate that the load versus crack extension responses and the calibrated value of β_{met} exhibit only small sensitivity to q over the range of values considered. In summary, the determined cohesive parameters for the TiB/Ti FGM are $\Gamma_{\text{met}}^c = 24$ kJ/m², $\sigma_{\text{met}}^c = 2.5\sigma_0$ (1125 MPa), $\delta_{\text{met}}^c = 0.008$ mm, $\Gamma_{\text{cer}}^c = 0.11$ kJ/m², $\sigma_{\text{cer}}^c = 4$ MPa, $\delta_{\text{cer}}^c = 0.01$ mm, $\beta_{\text{met}} = 18.5$ and $\beta_{\text{cer}} = 1$.

5.4. Crack tunneling in Ti SE(B) specimen

Although the initial crack front is straight in analyses of the Ti SE(B) specimen, the extended crack front exhibits a strong tunneling effect, i.e. the crack extends deeper in the interior part than at the outside surface of the specimen. Sufficient plastic deformation exists at the crack initiation load to develop strong gradients of opening displacement along the initial crack front with a maximum value at the center-plane. Fig. 16 shows the opening displacement along the initial straight crack front of the SE(B) specimen at the crack initiation load. The displacement reaches 0.045 mm at the mid-plane and decreases to 0.012 mm at the outside surface. The opening displacement near the outside surfaces will reach $5\delta_{\text{met}}^c$ (element extinction and crack growth condition) only after the crack grows ahead in the interior part thereby decreasing the remaining ligament area.

Fig. 17 shows the tunneling development predicted in the Ti SE(B) specimen at different load levels. The crack initiates first over the middle portion of the specimen (Fig. 17(a)). After extending $\Delta a_i = 2.5$ mm (19% of the specimen thickness) at the interior mid-plane, the crack starts to grow at the outside surface (Fig. 17(b)). Fig. 17(c) shows the crack front profile at a relatively advanced stage. The crack extensions at the outside surface and the mid-plane are $\Delta a_s = 0.4$ mm and $\Delta a_i = 4.4$ mm, respectively. The study of Roy and Dodds [16] using a 3-D cohesive zone model for crack growth in thin (2.3 mm) aluminum sheets shows that

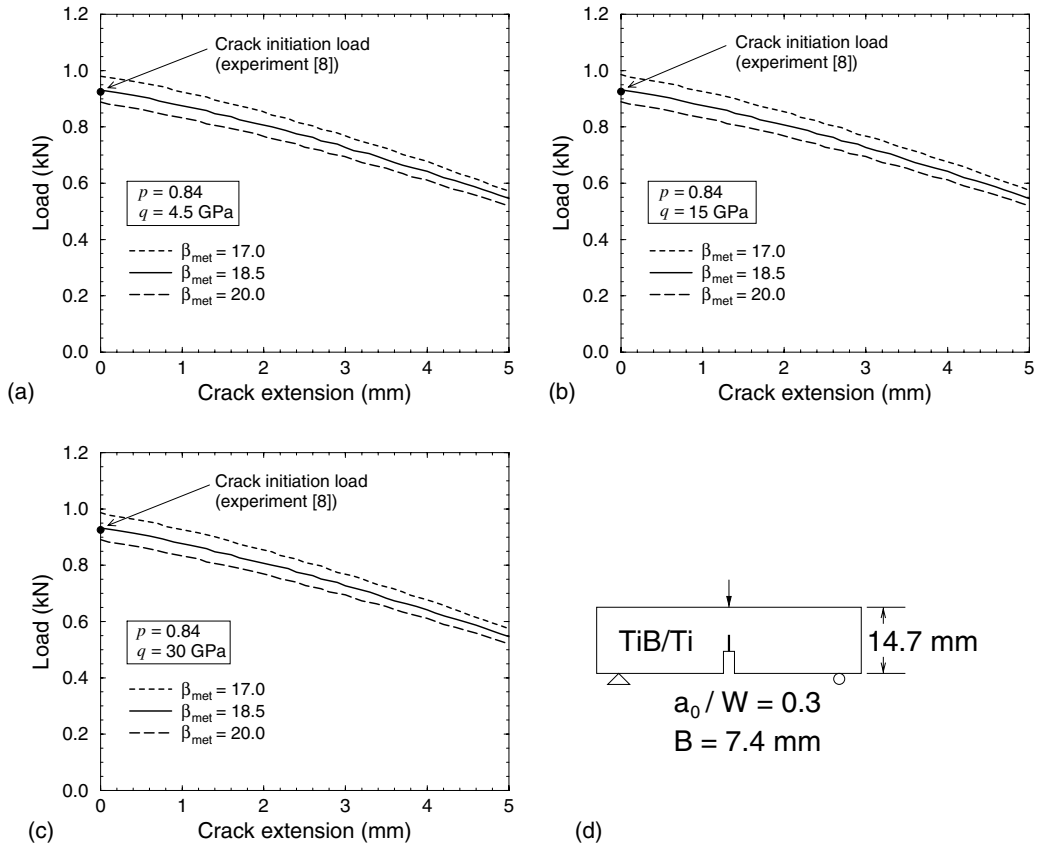


Fig. 15. Calibration of β_{met} using the crack initiation load for the TiB/Ti SE(B) specimen with $W = 14.7$ mm; (a) $q = 4.5$ GPa; (b) $q = 15$ GPa; (c) $q = 30$ GPa; (d) specimen.

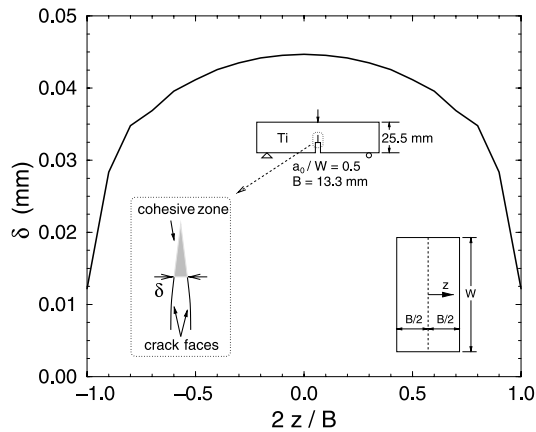


Fig. 16. Opening displacement profile along the crack front of the Ti SE(B) specimen at the crack initiation load (element extinction occurring at an element-averaged $\delta = 5\delta_{met}^c = 0.042$ mm).

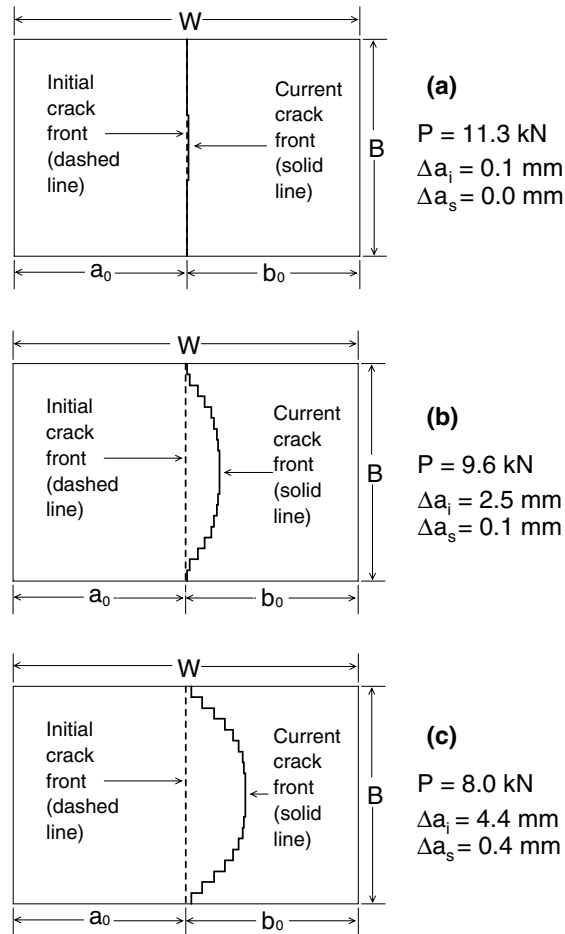


Fig. 17. Crack tunneling in the Ti SE(B) specimen with $W = 25.5 \text{ mm}$; (a) crack initiation at the mid-plane; (b) crack initiation at the outside surface; (c) an advanced stage of crack growth with extensions of 0.4 and 4.4 mm at the outside surface and mid-plane, respectively.

the crack front attains a steady profile once crack extension at the surface reaches $\approx 1 \times$ the plate thickness. For the SE(B) specimen studied here, the crack growth likely does not reach a steady state because the initial ligament size ($b_0 = 12.75 \text{ mm}$) nearly equals the specimen thickness ($B = 13.3 \text{ mm}$).

Fig. 18 compares the predicted crack front profile with the experimentally observed one [39] (which was obtained by post-test fatigue cycling using a load ratio of $R = 0.5$). The experimental crack front with the crack extensions of about 3.1 and 8.1 mm at the surface and the mid-plane, respectively, can be approximately captured by the analyses with the predicted crack extensions of 3.1 and 7.7 mm, respectively.

5.5. Crack growth in TiB/Ti FGM SE(B) specimens

We now study crack growth in the TiB/Ti FGM SE(B) specimen to investigate the effect of a range of values for the metal volume fraction exponent p (in Eq. (32)) on the crack growth behavior with the calibrated cohesive parameters. The q parameter in the TTO model is taken as 4.5 GPa in all calculations—the

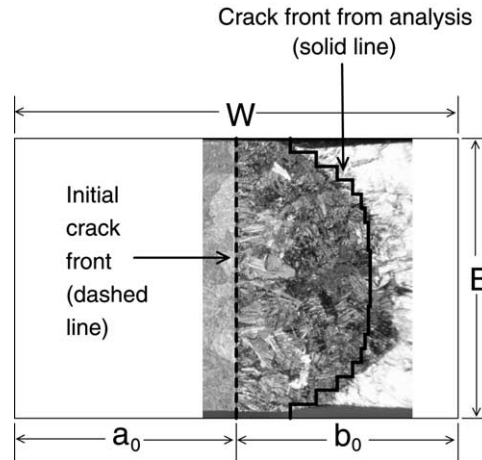


Fig. 18. Crack front in the Ti SE(B) specimen with $W = 25.5$ mm: experiment [39] (right edge of the shaded area with approximate extensions of 3.1 and 8.1 mm at the outside surface and the mid-plane, respectively), and simulation (heavy solid line with extensions of 3.1 and 7.7 mm at the outside surface and the mid-plane, respectively).

load versus crack extension responses exhibit only small sensitivity to q (see results and discussion in Section 5.3.2).

Fig. 19 shows the load versus crack extension curves for various values of p with the model parameters determined in Sections 5.3.1 and 5.3.2. The layered TiB/Ti specimen tested in [8] is modeled by a continuously graded TiB/Ti with $p = 0.84$. The solid lines describe the crack growth behavior at the mid-plane and the dashed lines at the outside surface. Almost no differences between the crack extensions at the surface and mid-plane are observed, i.e. no crack tunneling develops for crack growth in this FGM specimen. For a given p , the load decreases steadily with crack extension. This is the behavior also exhibited for the pure Ti specimen. The load at fixed crack extension decreases with increasing p . A larger p cor-

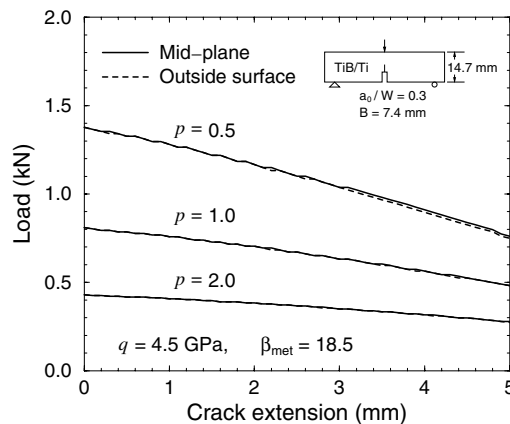


Fig. 19. Load versus crack extension responses for the TiB/Ti SE(B) specimen with $a_0/W = 0.3$, $B = 7.4$ mm, $q = 4.5$ GPa, $\beta_{\text{met}} = 18.5$. Essentially no tunneling develops in this specimen.

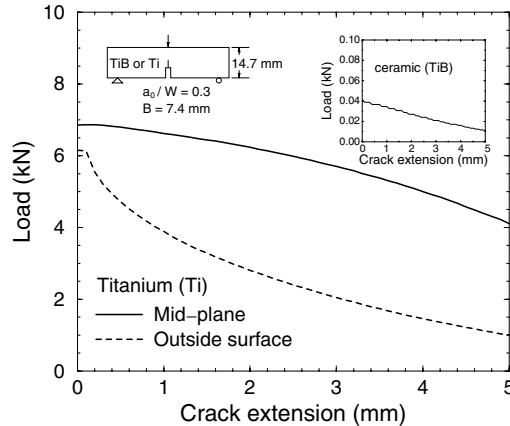


Fig. 20. Load versus crack extension responses for both the Ti and TiB SE(B) specimens with $a_0/W = 0.3$ and $B = 7.4$ mm. These two configurations provide bounding solutions for the TiB/Ti FGM responses.

responds to a lower metal volume fraction, which leads to a lower cohesive traction and energy for the FGM.

Fig. 20 shows the load versus crack extension curves for SE(B) specimens geometrically identical to those in Fig. 19 but now made of Ti only and TiB only, respectively. These two additional configurations provide bounding solutions for the TiB/Ti FGM responses. At specified crack extensions, the load for the Ti specimen remains much larger than those for the TiB/Ti FGM specimens with various values of p . For example, the crack initiation load is 6.86 kN for the Ti specimen, and 1.38, 0.81 and 0.43 kN for the FGM specimen when p takes values of 0.5, 1.0 and 2.0, respectively. The loads during crack extension for the pure TiB, however, remain at least one order of magnitude smaller than those for the FGM specimen (see insert in Fig. 20).

For the Ti specimen, Fig. 20 shows strong crack tunneling—the crack growth initiates at the outside surface only after it has already extended about 2.1 mm at the mid-plane (28% of the specimen thickness and the load reduced to 6.1 kN). This behavior is in sharp contrast to that for the FGM specimen which shows essentially no crack tunneling. Crack tunneling results from strong gradients of stress parallel to the crack front that develop with extensive plastic deformation in ductile materials. In comparison, the present TiB/Ti FGM is relatively brittle. The critical J -integral, J_{IC} , for the TiB/Ti composite is only 0.28 and 1.59 kJ/m² when the volume fraction of the Ti is 68% and 85%, respectively [39], while the J at the crack initiation is 24 kJ/m² for the pure Ti (100% Ti).

Though this specific FGM SE(B) specimen shows little crack tunneling, other FGM systems or the TiB/Ti systems obtained under different fabrication conditions may exhibit pronounced tunneling phenomenon if significant plastic deformation develops. For example, Fig. 21 shows the load versus crack extension responses for the TiB/Ti FGM specimen with $p = 0.3$ (metal-rich) and relatively smaller β_{met} values (this may be achieved by carefully controlling the microstructure of the material during the fabrication process). Fig. 21 shows that significant crack tunneling develops for $\beta_{met} = 2$ and crack tunneling becomes less pronounced with increasing values of β_{met} .

5.6. Effect of peak cohesive traction for ceramic phase

In the above study of crack extension in the TiB/Ti SE(B) specimen, we have proposed that selection of the peak cohesive traction for the ceramic phase, σ_{cer}^c , does not play a significant role in crack growth

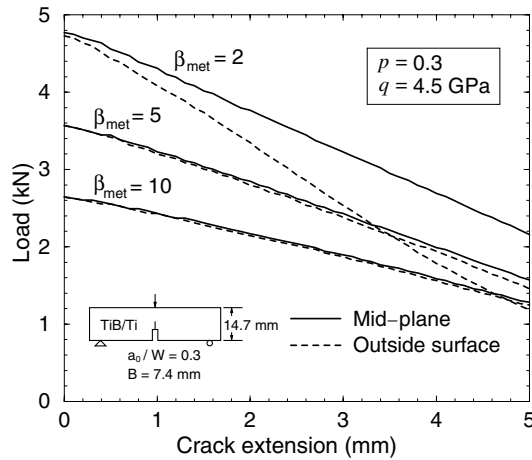


Fig. 21. Load versus crack extension responses for the TiB/Ti SE(B) specimen with $a_0/W = 0.3$, $B = 7.4$ mm ($q = 4.5$ GPa, $p = 0.3$).

behavior of ceramic/metal FGMs at an engineering-scale (millimeters of growth). The cohesive energy density of the ceramic, Γ_{cer}^c , is usually at least two orders of magnitude smaller than that of the metal, Γ_{met}^c . σ_{cer}^c , however, may affect the initial stiffness of the FGM cohesive zone model (21)–(23). Fig. 22 shows the calculated load versus CMOD curves for two values of σ_{cer}^c (4 and 60 MPa), as well as the response for a stationary crack model without cohesive elements. For the stationary crack model, the load increases with the increasing CMOD almost linearly in the range of loads considered indicating little plastic deformation in the background material before crack initiation. In contrast, the model with $\sigma_{cer}^c = 4$ MPa has a non-linear load versus CMOD response even at very low load levels. The load first increases with increasing CMOD, reaches a peak value of about 1 kN, and then decreases with further increasing CMOD. The crack initiation corresponding to $\delta_{eff} = 5\delta_{met}^c$, however, does not occur at the peak load. The crack starts to grow

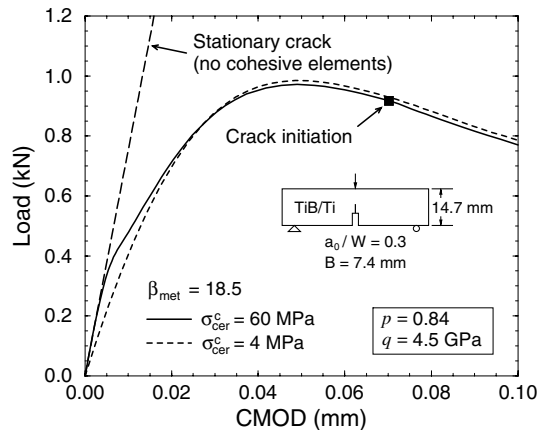


Fig. 22. Computed load versus CMOD curves for the TiB/Ti SE(B) specimen with $W = 14.7$ mm: effect of peak cohesive traction of ceramic phase, σ_{cer}^c .

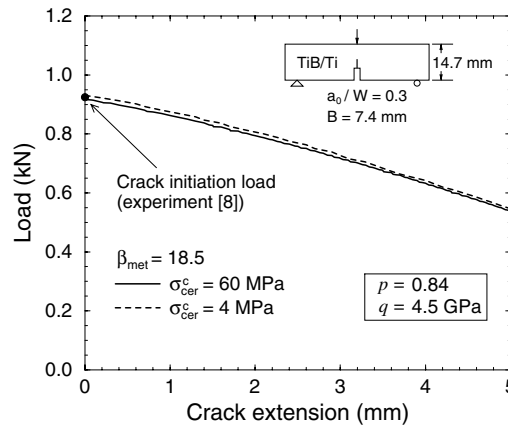


Fig. 23. Load versus crack extension responses for the TiB/Ti SE(B) specimen with $a_0/W = 0.3$, $B = 7.4$ mm: effect of peak cohesive traction of ceramic phase, σ_{cer}^c .

after the load passes the peak value. This behavior differs from the Ti metal shown in Fig. 12 and develops from the relative brittleness of the TiB/Ti FGM discussed in Section 5.5. For brittle materials which exhibit softening cohesive behavior, size effects play a strong role in determining the peak and crack initiation loads. The crack initiation load is usually lower than the peak load level and crack growth initiates after the load passes the peak value [25].

The initial slope of the load versus CMOD curve for the cohesive model with $\sigma_{cer}^c = 4$ MPa is smaller than the slope for the stationary crack model. Thus, the stiffness of the cohesive zone with $\sigma_{cer}^c = 4$ MPa does not compare with the slope of the undamaged material at the initial loading stage. For an increased value of σ_{cer}^c to 60 MPa (other cohesive parameters for the ceramic remain the same), the load versus CMOD response initially follows the stationary crack response and then closely follows the response for the model with $\sigma_{cer}^c = 4$ MPa. Fig. 23 shows the load versus average crack extension curves for $\sigma_{cer}^c = 4$ and 60 MPa. For a given crack extension, the load for $\sigma_{cer}^c = 4$ MPa is just slightly higher than that for $\sigma_{cer}^c = 60$ MPa. These results suggest that the peak cohesive traction of the ceramic does affect the initial stiffness of the cohesive material but does not significantly influence the extended crack growth response. The initially intact FGM ahead of the crack undergoes early damage in the ceramic phase but the metal phase eventually controls the complete separation of the FGM and the crack growth behavior.

6. Concluding remarks

This study employs a new phenomenological cohesive zone model [18] and extends the TTO model [9] within a 3-D computational framework that includes graded solid and interface-cohesive elements to investigate elastic–plastic crack growth in Ti metal and TiB/Ti FGM SE(B) specimens. The cohesive zone model involving six material-dependent parameters (the cohesive energy densities and the peak cohesive tractions of the ceramic and metal phases, respectively, and two cohesive gradation parameters) describes the constitutive behavior of the cohesive material and the TTO model characterizes the elastic–plastic response of the bulk background material. The finite element analyses of crack growth in the SE(B) specimens show that:

- (1) calibration of the cohesive zone model using the experimental load versus crack extension responses for a Ti SE(B) specimen yields a cohesive energy density of $\Gamma_{\text{met}}^c = 24 \text{ kJ/m}^2$ and a peak cohesive traction of $\sigma_{\text{met}}^c = 2.5\sigma_0$ (1125 MPa) for the Ti metal;
- (2) calibration of the cohesive zone model using the experimental crack initiation load for a TiB/Ti SE(B) specimen yields a cohesive gradation parameter of $\beta_{\text{met}} = 18.5$ for the TiB/Ti FGM;
- (3) the load versus crack extension responses and the calibrated β_{met} for the TiB/Ti FGM exhibit only small sensitivity to the parameter q in the TTO model when q is in the range of 4.5–30 GPa;
- (4) the load decreases steadily with the crack extension for both Ti metal and TiB/Ti FGM SE(B) specimens having a thickness to depth ratio (B/W) of around 0.5;
- (5) the peak cohesive traction of the ceramic phase influences the initial stiffness of the cohesive zone but only slightly affects the load versus crack extension responses for the TiB/Ti FGM;
- (6) the 3-D models predict strong crack tunneling in the Ti metal SE(B) specimen.

The numerical analyses capture the experimentally observed tunneled crack front profile in the Ti specimen with reasonable accuracy. For the TiB/Ti FGM SE(B) specimen, significant crack tunneling develops for $\beta_{\text{met}} = 2$ and crack tunneling becomes less pronounced with increasing values of β_{met} . In particular, no crack tunneling is observed for the FGM specimen with the calibrated β_{met} value (18.5). Crack tunneling accompanies strong through-thickness stress gradients that develop under extensive plastic deformation—the present TiB/Ti FGM with the calibrated β_{met} value (18.5) is relatively brittle.

The work described here represents exploratory developments in the modeling of ductile fracture processes in ceramic/metal FGMs at engineering scales. The scarcity of experimental data for these new materials does not yet support some recommendations for specific details adopted in the phenomenological models of the type proposed here. Issues including the effects of cohesive curve shapes for the ceramic and metal constituents, the effects of crack-front triaxiality on the cohesive parameters and the functional forms for the β_{met} and β_{cer} type parameters remain unresolved. Applications of the present cohesive zone model to study ductile failure of ceramic/metal FGMs require further experimental verification and validation.

Acknowledgements

This work was supported by the NASA-Ames “Engineering for Complex System Program”, and the NASA-Ames Chief Engineer’s Office (Dr. Tina Panontin) through grant NAG 2-1424. Additional support for this work was provided by the National Science Foundation (NSF) under grant CMS-0115954 (Mechanics & Materials Program).

References

- [1] Hirai T. Functionally gradient materials. In: Brook RJ, editor. Processing of ceramics, Part 2. Materials science and technology, vol. 17B. Weinheim, Germany: VCH Verlagsgesellschaft mbH; 1996. p. 292–341.
- [2] Suresh S, Mortensen A. Functionally graded materials. London: The Institute of Materials, IOM Communications Ltd.; 1998.
- [3] Paulino GH, Jin ZH, Dodds Jr RH. Failure of functionally graded materials. In: Karihaloo B, Knauss WG, editors. Comprehensive structural integrity, vol. 2. Oxford: Elsevier Science Limited; in press [chapter 13].
- [4] Jin ZH, Batra RC. Some basic fracture mechanics concepts in functionally graded materials. J Mech Phys Solids 1996;44:1221–35.
- [5] Cai H, Bao G. Crack bridging in functionally graded coatings. Int J Solids Struct 1998;35:701–17.
- [6] Eischen JW. Fracture of nonhomogeneous materials. Int J Fract 1987;34:3–22.
- [7] Jin ZH, Noda N. Crack-tip singular fields in nonhomogeneous materials. ASME J Appl Mech 1994;61:738–40.
- [8] Carpenter RD, Liang WW, Paulino GH, Gibeling JC, Munir ZA. Fracture testing and analysis of a layered functionally graded Ti/TiB beam in 3-point bending. Mater Sci Forum 1999;308–311:837–42.

- [9] Tamura I, Tomota Y, Ozawa H. Strength and ductility of Fe–Ni–C alloys composed of austenite and martensite with various strength. In: *Proceedings of the Third International Conference on Strength of Metals and Alloys*, vol. 1. Cambridge: Institute of Metals; 1973. p. 611–5.
- [10] Williamson RL, Rabin BH, Drake JT. Finite element analysis of thermal residual stresses at graded ceramic–metal interfaces, Part I: model description and geometrical effects. *J Appl Phys* 1993;74:1310–20.
- [11] Giannakopoulos AE, Suresh S, Finot M, Olsson M. Elastoplastic analysis of thermal cycling: layered materials with compositional gradients. *Acta Metall Mater* 1995;43:1335–54.
- [12] Dugdale DS. Yielding of steel sheets containing slits. *J Mech Phys Solids* 1960;8:100–4.
- [13] Hillerborg A, Modeer M, Petersson PE. Analysis of crack formation and crack growth in concrete by means of fracture mechanics and finite elements. *Cem Concr Res* 1976;6:773–82.
- [14] Mosalam KM, Paulino GH. Evolutionary characteristic length method for smeared cracking finite element models. *Finite Elem Anal Des* 1997;27:99–108.
- [15] Needleman A. A continuum model for void nucleation by inclusion debonding. *ASME J Appl Mech* 1987;54:525–31.
- [16] Roy YA, Dodds Jr RH. Simulation of ductile crack growth in thin aluminum panels using 3-D surface cohesive elements. *Int J Fract* 2001;110:21–45.
- [17] Finot M, Shen YL, Needleman A, Suresh S. Micromechanical modeling of reinforcement fracture in particle-reinforced metal–matrix composites. *Metall Trans* 1994;25A:2403–20.
- [18] Jin ZH, Paulino GH, Dodds Jr RH. Finite element investigation of quasi-static crack growth in functionally graded materials using a novel cohesive zone fracture model. *ASME J Appl Mech* 2002;69:370–9.
- [19] Paulino GH, Carpenter RD, Liang WW, Munir ZA, Gibeling JC. Fracture testing and finite element modeling of pure titanium. *Engng Fract Mech* 2001;68:1417–32.
- [20] Camacho GT, Ortiz M. Computational modelling of impact damage in brittle materials. *Int J Solids Struct* 1996;33:2899–938.
- [21] Rose JH, Ferrante J, Smith JR. Universal binding energy curves for metals and bimetallic interfaces. *Phys Rev Lett* 1981;47:675–8.
- [22] Siegmund T, Needleman A. A numerical study of dynamic crack growth in elastic–viscoplastic solids. *Int J Solids Struct* 1997;34:769–88.
- [23] Ortiz M, Pandolfi A. Finite-deformation irreversible cohesive elements for three-dimensional crack-propagation analysis. *Int J Numer Meth Engng* 1999;44:1267–82.
- [24] Tvergaard V, Hutchinson JW. The relation between crack growth resistance and fracture process parameters in elastic–plastic solids. *J Mech Phys Solids* 1992;40:1377–92.
- [25] Guinea GV, Elices M, Planas J. On the initial shape of the softening function of cohesive materials. *Int J Fract* 1997;87:139–49.
- [26] Roychowdhury S, Roy YDA, Dodds Jr RH. Simulation of ductile tearing in thin aluminum panels using large-displacement interface-cohesive elements. *Engng Fract Mech* 2002;69:983–1002.
- [27] Cook RD, Malkus DS, Plesha ME. *Concepts and applications of finite element analysis*. 3rd ed. New York: John Wiley and Sons; 1989.
- [28] Hughes TJR. Generalization of selective integration procedures to anisotropic and nonlinear media. *Int J Numer Meth Engng* 1980;15:1413–8.
- [29] Nakamura T, Shih CF, Freund LB. Analysis of dynamically loaded SE(B) ductile fracture specimen. *Engng Fract Mech* 1986;25:323–39.
- [30] Kim JH, Paulino GH. Finite element evaluation of mixed mode stress intensity factors in functionally graded materials. *Int J Numer Meth Engng* 2002;52:1903–35.
- [31] ABAQUS/standard user's manual, vol. II, version 6.2. Hibbitt, Karlsson & Sorensen, Inc, 1080 Main Street, Pawtucket, RI 02860-4847, USA.
- [32] Kim JH, Paulino GH. Isoparametric graded finite elements for nonhomogeneous isotropic and orthotropic materials. *ASME J Appl Mech* 2002;69:502–14.
- [33] Nelson G, Ezis A. Functionally graded material (FGM) armor in the TiB/Ti system (U). CERCOR Report, Vista, CA 92083, USA, 1996.
- [34] Gullerud AS, Koppenhoefer KC, Roy YA, Dodds Jr RH. WARP3D—Release 13.8 manual. Civil Engineering, Report No. UILU-ENG-95-2012, University of Illinois, Urbana, IL 61801, USA, 2000.
- [35] Anlas G, Santare MH, Lambros J. Numerical calculation of stress intensity factors in functionally graded materials. *Int J Fract* 2000;104:131–43.
- [36] Nevalainen M, Dodds Jr RH. Numerical investigation of 3-D constraint effects on brittle fracture in SE(B) and C(T) specimens. *Int J Fract* 1995;74:131–61.
- [37] Dodds Jr RH, Shih CF, Anderson TL. Continuum and micro-mechanics treatment of constraint in fracture. *Int J Fract* 1993;64:101–33.

- [38] Liang WW. Finite element analysis of model I crack propagation in layered functionally graded materials. MSc thesis, University of California, Davis, CA, USA, 1999.
- [39] Carpenter RD. Experimental fracture measurements of functionally graded materials. PhD thesis, University of California, Davis, CA, USA, 2002.